

Journal of Materials Chemistry A

Materials for energy and sustainability

rsc.li/materials-a



ISSN 2050-7488



PAPER

Hyunwoong Park *et al.*

Facilitating hole transfer on electrochemically synthesized p-type CuAlO_2 films for efficient solar hydrogen production from water

Cite this: *J. Mater. Chem. A*, 2017, 5, 10165

Facilitating hole transfer on electrochemically synthesized p-type CuAlO₂ films for efficient solar hydrogen production from water†

Seung Yo Choi,^{ab} Chang-Duk Kim,^c Dong Suk Han^d and Hyunwoong Park^{id} ^{*abe}

Delafossite CuAlO₂ photoelectrodes are synthesized *via* the electrodeposition of Cu(II) and Al(III) onto fluorine-doped tin oxide (FTO) substrates in water and dimethylsulfoxide (DMSO) solvents, followed by annealing in air and Ar. The surface properties, crystalline structure, and photoelectrochemical (PEC) performance of the as-synthesized samples are significantly affected by the synthetic conditions. Optimized CuAlO₂ electrodes (synthesized in DMSO and annealed in air) possess suitable energetics for H₂ production under sunlight (an optical bandgap of ~1.4 eV and a conduction band level of -0.24 V_{RHE}). They exhibit a photocurrent onset potential of ~+0.9 V_{RHE} along with a faradaic efficiency of ~70% at +0.3 V_{RHE} in an alkaline solution (1 M KOH) under simulated sunlight (AM 1.5; 100 mW cm⁻²). The addition of sacrificial hole scavengers (sulfide and sulfite) significantly improves the PEC performance of CuAlO₂ by a factor of eight, along with providing a faradaic efficiency of ~100%. This indicates that the hole transfer limits the overall PEC performance. This issue is addressed by employing a ~150 nm-thick Au film-coated FTO substrate for the CuAlO₂ deposition. In the absence of hole scavengers, the H₂ production with the Au-underlain CuAlO₂ photoelectrode (Au/CuAlO₂) is three-fold higher than that with bare CuAlO₂, while the faradaic efficiencies at +0.3 and +0.55 V_{RHE} are ~100%. The time-resolved photoluminescence emission decay spectra of the CuAlO₂ and Au/CuAlO₂ confirm the facilitated charge transfer in the latter.

Received 2nd March 2017
Accepted 5th April 2017

DOI: 10.1039/c7ta01919j

rsc.li/materials-a

1. Introduction

The semiconductor-based solar production of carbon-neutral chemicals (*e.g.*, H₂ and formate from water and CO₂, respectively) has been studied over the past four decades,^{1–4} but has recently received greater attention because of the increase in the concentration of atmospheric CO₂ beyond 400 ppm. There are numerous semiconductors available, including oxides,^{5–9} chalcogenides,^{10–13} silicon,^{14–16} and III–V composites.^{3,17} However, they often suffer from low efficiency, a complicated synthetic process, the use of expensive components, non-scalability, and low durability. Cu(I)-based delafossite materials are unique in terms of their structure (Cu^IM^{III}O₂ type, where M = Fe,^{18–21} Rh,²² Al,^{23,24} Ga,²⁵ *etc.*); various bandgap (E_g) energies (1.2–3.0 eV);

high conduction band (E_{cb}) level, which is sufficient for H₂ production and CO₂ reduction; and relative stability in aqueous solutions compared to other p-type III–V and II–VI materials.^{26,27} For example, electrodeposited *p*-CuFeO₂ ($E_g \sim 1.36$ eV) was shown to be capable of producing H₂ in an aqueous alkaline solution,²⁸ whereas intercalating Mg²⁺ or oxygen atoms into CuFeO₂ enhanced the photoelectrochemical (PEC) performance.¹⁸ Furthermore, CuFeO₂ coupled with CuO ($E_g \sim 1.4$ eV) could produce formate from CO₂ and water at a circumneutral pH with a ~1% energy efficiency in the absence of any potential bias.^{29–31}

In comparison to CuFeO₂, CuAlO₂ has been given less attention despite their similar physicochemical properties. The typical synthetic route of CuAlO₂ is annealing a Cu(I) and Al(III) salt mixture at high temperature (solid-solution process),^{23,26} which results in irregular, coarse particles of several micrometers.^{18,25} Although this method has some advantages (*e.g.*, high yield), the as-synthesized particles are difficult to fabricate into durable films on transparent conducting oxide (TCO) substrates because of the absence of particle-to-particle interaction. Even if they are formed, the films have less intimate and looser inter-particle connections undergoing a significant charge recombination at the solid/solid interface.^{18,23} This difficulty in synthesizing CuAlO₂ films has caused this material to be less studied despite its potential as a promising photocathode.

^aSchool of Energy Engineering, Kyungpook National University, Daegu 41566, Korea. E-mail: hwp@knu.ac.kr; Tel: +82-53-950-8973

^bSchool of Architectural, Civil, Environmental, and Energy Engineering, Kyungpook National University, Daegu 41566, Korea

^cDepartment of Physics, Kyungpook National University, Daegu 41566, Korea

^dChemical Engineering Program, Texas A&M University at Qatar, Education City, P.O. Box 23874, Doha, Qatar

^eAdvanced Institute of Water Industry, Kyungpook National University, Daegu 41566, Korea

† Electronic supplementary information (ESI) available: Fig. S1–S12. See DOI: 10.1039/c7ta01919j



With this in mind, we have, for the first time, attempted to synthesize CuAlO₂ films on TCO substrates *via* electrochemical deposition (ED) under various experimental conditions (*e.g.*, ED potentials, times, solution media, and annealing atmospheres). The as-synthesized CuAlO₂ samples were characterized using various surface analysis tools (SEM, EDX, XRD, XPS, UV-vis, impedance, and time-resolved fluorescence spectrometry). They were then further evaluated in terms of their PEC hydrogen production in aqueous alkaline solutions under simulated sunlight (AM 1.5; 1 sun). The results of this evaluation showed that the hole transfer limited the overall PEC performance, and the use of sacrificial hole scavengers (electron donors) significantly improved the H₂ production. To address this issue, thin Au layers (~150 nm), as a hole conductor, were pre-deposited onto TCO substrates *via* an electron-beam evaporation system to facilitate the hole transfer of CuAlO₂. In the absence of the hole scavengers, the H₂ production with the Au-underlain CuAlO₂ photoelectrode (Au/CuAlO₂) was three-fold higher than that with bare CuAlO₂, while the faradaic efficiencies were ~100%.

2. Experimental

2.1. Synthesis of samples

Pieces of fluorine-doped SnO₂ (F:SnO₂, FTO)-coated glass (Pilkington Co, 1 cm × 3 cm) were ultrasonically cleaned in ethanol for 10 min, rinsed with deionized water (>18 MΩ cm, Barnstead), and dried in an N₂ stream. For the electrochemical plating of Cu and Al, the as-prepared FTO (working electrode), saturated calomel electrode (SCE, reference electrode), and Pt wire (counter electrode) were immersed in a deionized water or dimethylsulfoxide (DMSO, >99%, Wako) solution containing Cu(NO₃)₂·3H₂O (4 mM, >99%, Sigma Aldrich), Al(NO₃)₃·9H₂O (20 mM, >98%, Sigma Aldrich), and KClO₄ (50 mM, >99%, Sigma Aldrich). Then, the FTO substrates were held at constant potentials (−0.31 V_{SCE} in water and −1.91 V_{SCE} in DMSO) for 2 h using a potentiostat/galvanostat (CompactStat, Ivium) (Fig. S1†). After the deposition, the samples were dried, washed with deionized water, and placed in a tube furnace (Ajeon Heating Industrial Co., LTD) at room temperature in the presence of atmospheric air or Ar. The furnace temperature was increased to 700 °C at a rate of 2 °C min^{−1} and held at 700 °C for 1 h. If necessary, Au-layered FTO (FTO/Au) was used for the deposition of CuAlO₂. For this, FTO substrates were coated with a 150 nm-thick Au layer using an electron-beam evaporation system (Dada Korea) with a metallic Au evaporation slug (99.999%) in a reactor chamber at a pressure of 2 × 10^{−5} Torr. The growth rate of the Au layer was estimated to be ~0.05 nm s^{−1}.³²

2.2. Photoelectrochemical measurements and product analysis

The as-synthesized samples (working electrodes) were immersed in aqueous potassium hydroxide (1 M KOH at pH ~13.5, Sigma Aldrich) pre-purged with N₂ for over 1 h in an airtight single (undivided) glass cell with an SCE (reference electrode) and a platinum wire (counter electrode). Light-chopped linear sweep

voltammograms were obtained *via* a potential sweep from +0.3 to −0.9 V_{SCE} at a scan rate of 5 mV s^{−1} under simulated solar light (100 mW cm^{−2}) from a 150 W xenon arc lamp (ABET Technology) equipped with an air mass (AM) 1.5G filter. The light intensity was weekly re-calibrated to be 1 sun (100 mW cm^{−2}) using a standard mono-Si solar cell (K801S-K009, McScience Inc.), as described elsewhere.³³ For the PEC H₂ production, constant potentials (−0.75 V_{SCE} and −0.5 V_{SCE}) were applied to the samples under irradiation. The potentials of the reference electrode (SCE) were converted to those of a reversible hydrogen electrode (RHE) using the following relationship:

$$V_{\text{RHE}} = V_{\text{SCE}} + 0.241 + 0.059 \times \text{pH}$$

Unless otherwise specified, the RHE was omitted for simplicity. The incident photon-to-current efficiency (IPCE) was estimated using a CS130 monochromator (Mmac-200, Spectro) with a 300 W Xe arc lamp using the following equation:

$$\text{IPCE (\%)} = \frac{1240 \times I_{\text{ph}} \text{ (mA cm}^{-2}\text{)}}{P_{\text{light}} \text{ (mW cm}^{-2}\text{)} \times \lambda \text{ (nm)}} \times 100\%$$

where I_{ph} , P_{light} , and λ refer to the photocurrent densities at 0.3 and 0.55 V, photon flux, and wavelength, respectively.

For quantification of molecular hydrogen (H₂) evolved, varying volumes (10–250 μL) of a standard H₂ gas (99.999%) with Ar carrier gas were flowed through a 5 Å molecular sieve column equipped in a gas chromatograph (GC, YoungLin, ACME-6100) with a thermal conductivity detector (TCD) (detection limit of H₂ ~ 0.01%), and a standard curve fit between the standard gas concentration and the corresponding spectral area was obtained. The faradaic efficiencies for H₂ under constant potentials were estimated using the following equation:

Faradaic efficiency (%) =

$$\frac{\text{H}_2 \text{ (mol)} \times (6.02 \times 10^{23})}{\int_0^t I_{\text{ph}} dt \times A \times 1/96485 \text{ C}^{-1} \text{ mol} \times t} \times 2 \times 100\%$$

where I_{ph} , A , and t are the photocurrent density (A cm^{−2}), area (0.25 cm²), and time (s), respectively. All of the photoelectrochemical experiments were repeated at least twice to obtain reliable results.

2.3. Surface characterization

The surface morphologies and side views of the samples were analyzed using a field-emission SEM (FE-SEM, Hitachi S4800) equipped with an energy-dispersive X-ray (EDX) detector. The UV-vis diffuse reflectance absorption spectra of the powders collected from the sample films were obtained using a UV-vis spectrophotometer (UV-2450, Shimadzu), with BaSO₄ as a ref. 29. The obtained reflectance (R) was then converted into absorbance *via* the Kubelka–Munk function $((1 - R)^2/2R)$.³⁴ X-ray diffraction (XRD) measurements were performed to examine the crystalline structures of the samples with a Philips X-pert powder diffractometer (PW3040/00) in a Bragg–Brentano geometry under Cu K α radiation. X-ray photoelectron



spectroscopy (XPS) and Auger spectroscopy (Cu LMM; XPS, ULVAC-PHI) analyses were performed on a PHI 5500 model spectrometer equipped with an Al K α monochromator X-ray source at 20 kV, a hemispherical electron energy analyzer, and a multichannel detector. The time-resolved photoluminescence (TRPL) lifetimes were measured using a confocal microscope (MicroTime-200, Picoquant, Germany) with a 20 \times objective. The measurements were performed at the Korea Basic Science Institute (KBSI), Daegu Center, South Korea. A single-mode pulsed diode laser (379 nm with a pulse width of \sim 30 ps and a laser power of \sim 30 μ W) was used as the excitation source. A dichroic mirror (Z375RDC, AHF), a long pass filter (HQ405lp, AHF), a 75 μ m pinhole, a band-pass filter, and an avalanche photodiode detector (PDM series, MPD) were used to collect emissions from the samples. The details of the measurements and data analysis can be found elsewhere.^{9,29,31,35}

3. Results and discussion

3.1. Electrochemical synthesis and characterization of CuAlO₂

Fig. 1 compares the light-chopped linear sweep voltammograms (LSVs) of samples that were electrochemically synthesized under diverse conditions. The sample deposited in the water solvent and annealed in an Ar atmosphere (water/Ar) showed a photocurrent onset potential (E_{on}) of \sim 0.9 V and a significant dark current of $E \sim$ 0.45 V. In addition, there was a cathodic peak at \sim 0.5 V, which was attributed to the reductions of Cu(I) and/or Cu(II) ($E^\circ(\text{Cu}^{2+}/\text{Cu}^+) = +0.153$ V; $E^\circ(\text{Cu}^+/\text{Cu}^0) = +0.521$ V). On the other hand, the sample deposited in water and annealed in an air atmosphere (water/air) exhibited a more anodic E_{on} (\sim 1.0 V) and yet large dark currents. The sample deposited in DMSO and annealed under Ar (DMSO/Ar) was poor at generating a photocurrent and suffered from a significant dark current. In contrast, the sample annealed in an air atmosphere (DMSO/air) displayed an E_{on} of \sim 0.9 V and a high photocurrent. Furthermore, a dark current started from $E \sim$ 0.42 V, indicating that the sample is more durable than the other samples. The DMSO/Ar sample was yellowish, whereas the other samples were blackish. This suggests that the latter three samples possess similar compositions and/or crystalline structures.

The XRD patterns of the as-synthesized samples were further examined to gain knowledge about the crystalline structures (Fig. 2a). Most of the XRD peaks in the water/Ar sample were indexed to CuAlO₂ (e.g., 006, 101, 012, 009, 018, and 112 planes at $2\theta = 32.5^\circ, 35.7^\circ, 38.8^\circ, 48.9^\circ, 57.1^\circ, \text{ and } 68.1^\circ$, respectively; JCPDS no. 73-9485), whereas there was a peak indexed to CuO (220) at $2\theta = 58.4^\circ$. The water/air sample exhibited the same XRD pattern. In the DMSO/air sample, CuAlO₂ peaks were predominant, whereas the intensity of CuO (220) was significantly reduced. It should be noted that the Cu(I) in the Cu-based delafossites (Cu^IM^{III}O₂) is readily oxidized to Cu(II) in the synthesis process and/or a partial oxidation of CuAlO₂ in air, leading to oxygen-enriched oxides.^{23,29,31} The presence of the mixed valence state of Cu(I) and Cu(II) usually increases the charge transfer.^{19,31,36,37} In contrast to these samples, the DMSO/Ar sample did not exhibit CuAlO₂ peaks, whereas only Al₂O₃-associated peaks

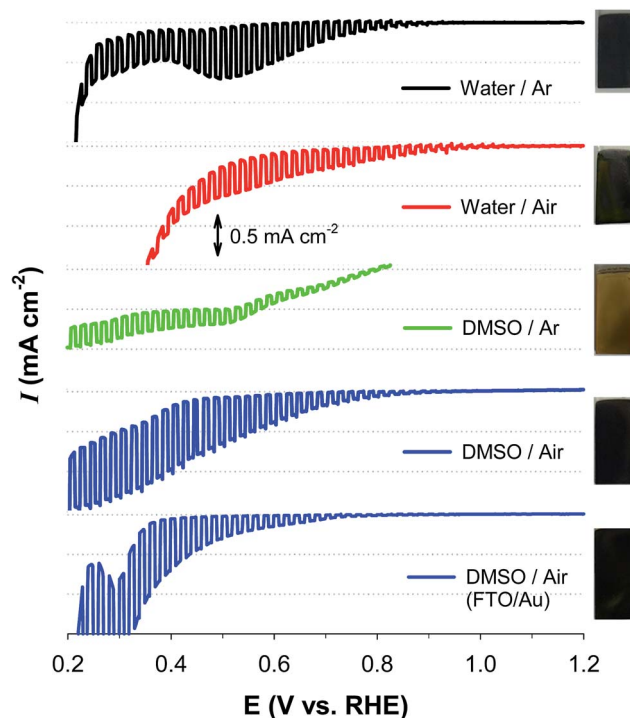


Fig. 1 Light-chopped linear sweep voltammograms (LSVs) of five sample electrodes synthesized via electrodeposition of Cu(II) and Al(III) onto FTO (omitted in legend) and FTO/Au in different solvents (water and DMSO) for 2 h followed by annealing in different atmospheres (air and Ar) at 700 $^\circ$ C. For example, DMSO/air refers to the sample deposited onto an FTO substrate in the DMSO solvent and annealed in an air atmosphere. Photos of the as-synthesized samples are shown on the right. FTO/Au refers to the FTO coated with a Au film (\sim 150 nm) via an electron-beam evaporation system. CuAlO₂ deposited onto the FTO/Au substrate is denoted as Au/CuAlO₂ in the text. To obtain the LSVs, the as-synthesized samples were immersed in an aqueous KOH solution purged with N₂ (1 M, pH \sim 13.5) under irradiation of AM 1.5 (100 mW cm⁻²).

(e.g., 111, 110, and 113 planes at $2\theta = 31.1^\circ, 36.7^\circ, \text{ and } 43.6^\circ$, respectively; JCPDS no. 75-0277) were found. This remarkable difference from the other samples was further confirmed by the yellowish color of the DMSO/Ar sample (Fig. 1).

Based on this knowledge, CuAlO₂ (i.e., the DMSO/air sample) was further analyzed using the XPS (Fig. 2b). The sample showed mixed bands at binding energies of 72 and 80 eV, the deconvolution of which indicated the co-presence of Al2p (73.6 eV) and Cu3p (74.9 and \sim 76.8 eV) at an atomic ratio of 1 : 1. The EDX analysis of the sample confirmed the similar composition ratio (Fig. S2[†]). In addition, the XPS O1s band could be resolved into a single oxygen atom coordinated to Cu(I) at 529.6 eV and two oxygen atoms coordinated to Al(III) (one from the AlO₆ edge-sharing octahedral layer at 530.8 eV and the other from a surface hydroxide or hydrated species at 531.9 eV) (Fig. S3[†]). Two satellite peaks in the Cu2p spectrum further suggested the existence of Cu(II) (Fig. 2b),³³ which was consistent with the results of the XRD analysis. The presence of Cu(II) was further confirmed by the XPS spectra of the Cu LMM Auger transition (Fig. 2b inset). The as-synthesized CuAlO₂ sample exhibited



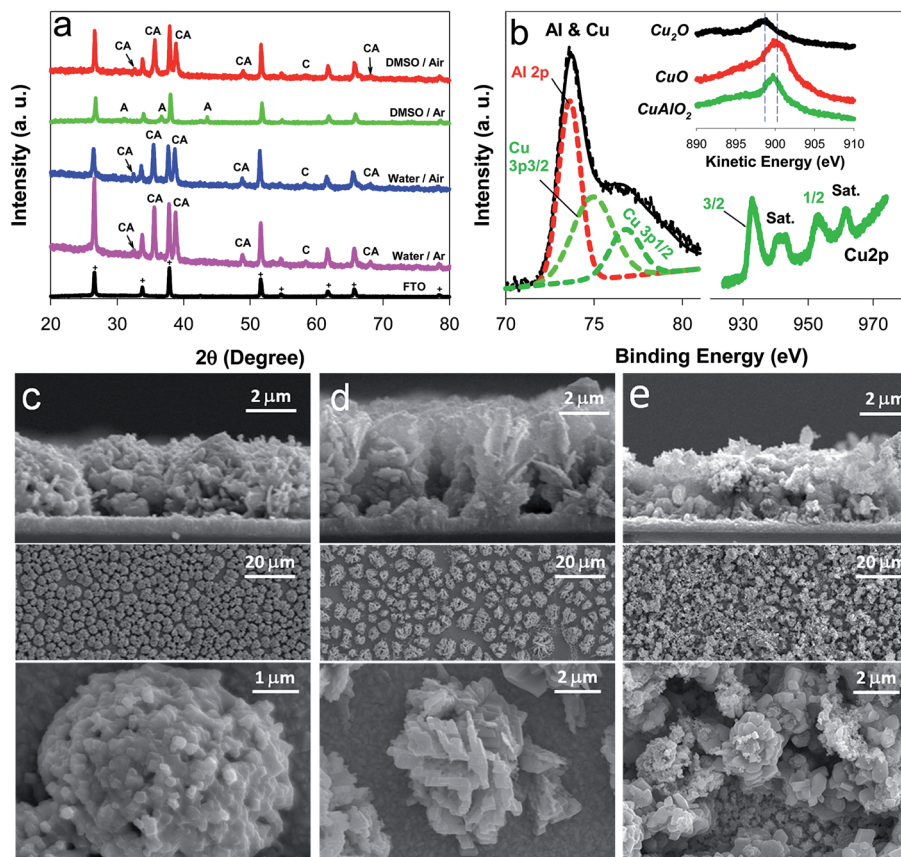


Fig. 2 Surface characterization of samples deposited onto FTO ((a) XRD, (b) XPS, and (c–e) SEM). In the XRD, CA, A, and C refer to CuAlO_2 , Al_2O_3 , and CuO , respectively (+originating from FTO). In the XPS of the DMSO/air samples, the left and right spectra show an Al2p and Cu3p mixed band (original and deconvoluted) and a Cu2p spectrum ($2p_{3/2}$, $2p_{1/2}$, and satellites), respectively, while the Cu LMM spectra of Cu_2O , CuO , and CuAlO_2 are compared in the inset. In the SEM, the cross-sectional and top views of (c) water/Ar, (d) water/air, and (e) DMSO/air are compared.

a kinetic energy peak at ~ 899.7 eV, which was located between those of Cu_2O (~ 898.8 eV) and CuO (~ 900.3 eV). The as-synthesized CuAlO_2 samples (*i.e.*, water/Ar, water/air, and DMSO/air) exhibited ~ 7 μm -thick porous particulate films composed of flower-like three-dimensional aggregates (Fig. 2c–e). This morphology is quite similar to those of electrochemically synthesized Cu-based oxide films (CuFeO_2 , CuO , Cu_2O , *etc.*),^{29–31} throughout which the component elements are uniformly distributed.^{29,31} The elemental mapping of the CuAlO_2 confirmed the uniform distribution of Cu and Al horizontally and vertically in the sample (Fig. S4[†]).

3.2. Use of CuAlO_2 for photoelectrochemical H_2 production

The PEC hydrogen evolution with CuAlO_2 (*i.e.*, DMSO/air sample) was systematically examined in an alkaline electrolyte (1 M KOH) with sulfide and/or sulfite (0.1 M Na_2S , 0.1 M Na_2SO_3 , and their mixed solution) as the sacrificial hole scavenger (Fig. 3a). It should be noted that sulfide and sulfite are typical products in the flue gas desulfurization processes of smelters and coal-fired power plants.³⁸ The overall shapes of the LSVs of the sulfide and sulfide/sulfite solutions were similar, with an E_{on} of ~ 0.85 V and a cathodic peak at ~ 0.45 V. When sulfite alone was present, a large dark current flowed at $E < \sim 0.7$ V, whereas no cathodic peak was found. This suggests that the

cathodic peak of CuAlO_2 could be attributed to sulfide, which has a higher reducing power ($E^\circ(\text{S}/\text{S}^{2-}) = -0.476$ V) than sulfite ($E^\circ(\text{S}_2\text{O}_6^{2-}/\text{H}_2\text{SO}_3) = 0.564$ V). Despite the cathodic peak of the mixed solution, the dark current was inhibited down to an E value of ~ 0.37 V, which was 0.1 V more negative than that in water (Fig. 1d *vs.* Fig. 3a). In the absence of the hole scavengers, the application of a potential at +0.55 V did not produce H_2 for 3 h despite a photocurrent flow. We could observe measurable amounts of H_2 (~ 2.5 μmol for 3 h) only at $E \leq +0.3$ V (Fig. 3b). A photocurrent of ~ 0.1 mA cm^{-2} was generated during the same period (Fig. S5[†]), leading to a Faraday efficiency of $\sim 70\%$ for H_2 production (Fig. 3c). In the presence of sulfite alone, the H_2 production and Faraday efficiency were enhanced yet insignificantly (~ 5 μmol for 3 h and $\sim 80\%$, respectively). However, the addition of sulfide to the water and sulfite solutions markedly enhanced the H_2 production by ~ 7 and ~ 4 times, with Faraday efficiencies of ~ 90 and $\sim 100\%$, respectively. Compared to sulfide alone, the higher efficiency of the sulfite/sulfide mixture was attributed to the regeneration of hole-oxidized sulfide (*e.g.*, S_2^{2-}) by sulfite.^{10–12,39} The Faraday efficiency of $\sim 100\%$ with bare CuAlO_2 in the mixed solution reveals that electron injection at the p-type material/water interface was highly efficient, whereas the internal hole transfer limited the overall charge transfer (see below). For comparison, the PEC activities of the other samples



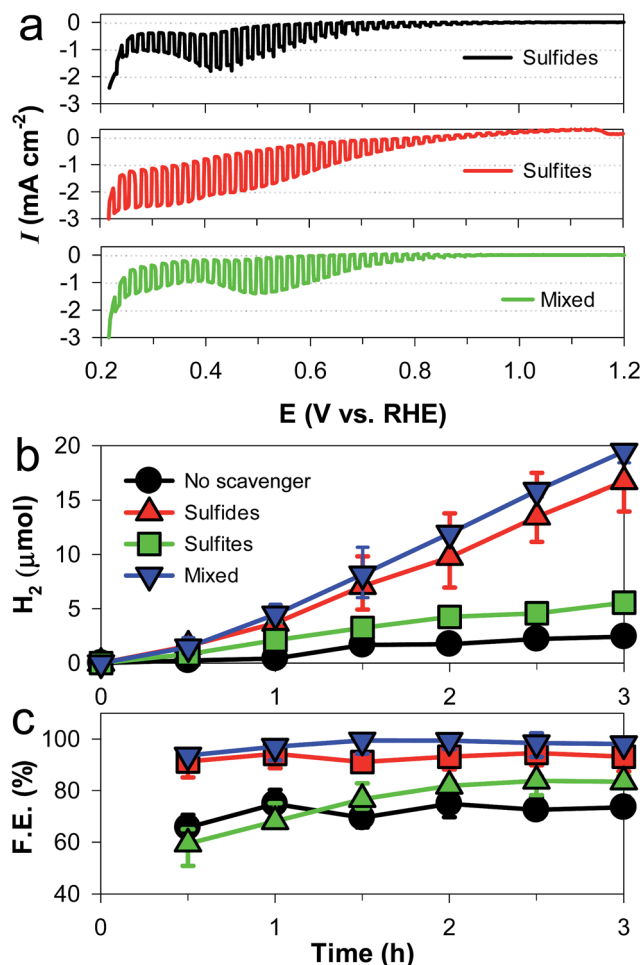


Fig. 3 Effects of hole scavengers (sulfide and/or sulfite, each 0.5 M) on the photoelectrochemical performance of CuAlO₂ electrodes in aqueous KOH solution (1 M) purged with N₂: (a) light-chopped LSVs, (b) H₂ production at +0.3 V_{RHE}, and (c) faradaic efficiencies (F. E.) for H₂ production at +0.3 V_{RHE}. "No scavenger" refers to 1 M KOH. See Fig. S5† for the photocurrent changes during the H₂ production tests.

(DMSO/Ar, water/Ar, and water/air) were examined in the mixed solution (Fig. S6†). The DMSO/Ar sample produced neither photocurrents nor H₂ at +0.3 V because of the predominant structure of Al₂O₃ (Fig. 2a). The other two samples with the

crystalline structure of CuAlO₂ exhibited the PEC activity; however, their H₂ production values were less than 5% of the production with the DMSO/air sample, and their faradaic efficiencies were less than 20%.

The energetics of the as-synthesized CuAlO₂ (*i.e.*, DMSO/air samples) were examined in detail. The UV-vis diffuse reflectance absorption spectrum of the CuAlO₂ particles (collected from the films) showed a broadband light absorption in the wavelength range of 400–900 nm, and the bandgap (E_g) was estimated to be ~1.4 eV (corresponding to a λ value of ~885 nm; see Fig. 4a). This E_g value was attributed to the indirectly allowed transition of CuAlO₂ (1.2–1.7 eV),^{23,40,41} whereas the directly allowed transition usually leads to large E_g values of 3–3.5 eV.^{24,27} The indirect transition-induced photogeneration of charge carriers was confirmed by the IPCE profiles (Fig. 4a). The IPCE value at $\lambda = 400$ nm was estimated to be ~15% ($E = +0.3$ V; see Fig. 1 for the photocurrent profile), which was not only far greater than the value reported in the literature (~0% at $\lambda > 400$ nm) for CuAlO₂ synthesized *via* a sol-gel process²⁴ but also >2-fold greater than those of other copper-based delafossites (*e.g.*, CuFeO₂ at $E = +0.15$ V) synthesized *via* the electrodeposition method.²⁹ In addition, the IPCE values decreased with increasing wavelength, with a wavelength onset of ~610 nm. A Mott-Schottky analysis of the as-synthesized CuAlO₂ film was performed at two frequencies (7 and 10 kHz) to estimate the flat band potential (E_{fb}) according to the following equation:⁴²

$$\frac{1}{C^2} = \frac{2}{\epsilon_0 \epsilon_r e N_D} \left(E - E_{fb} - \frac{kT}{e} \right)$$

where C , ϵ_0 , ϵ_r , N_D , E , k , and T refer to the space charge capacitance, permittivity of a vacuum, relative dielectric constant, donor density, applied potential, Boltzmann constant, and temperature, respectively. It should be noted that a decrease in $1/C^2$ with increasing potential bias is a characteristic of p-type semiconductors (Fig. 4b). The extrapolated x axis intercepts of the plots at the two frequencies coincided at $E \sim 1.25$ V, which corresponded to E_{fb} . Assuming that the valence band (VB) level was lower than E_{fb} by ~100 mV,⁴³ the conduction band (CB) of CuAlO₂ was determined to be -0.24 V, which is high enough to produce hydrogen from water ($E^\ominus = 0$ V) (Scheme 1a).

However, even though the energetics appeared to be suitable for PEC H₂ production, the as-synthesized CuAlO₂ generated

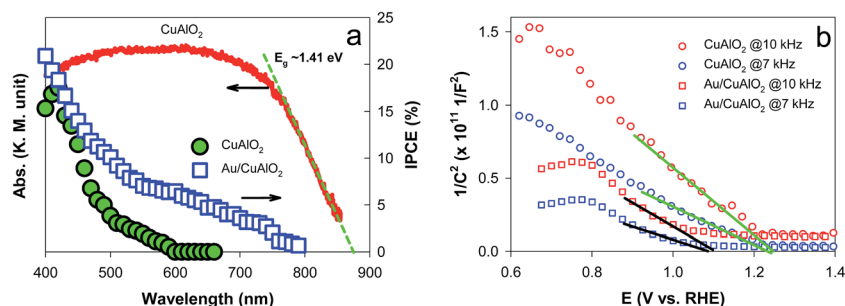
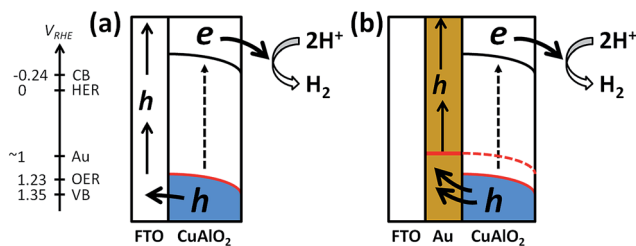


Fig. 4 (a) UV-vis diffuse reflectance absorption spectrum of CuAlO₂ particles (left) and incident photon-to-current efficiencies (IPCEs) of CuAlO₂ and Au/CuAlO₂ at +0.3 V_{RHE} in aqueous KOH solution (1 M) purged with N₂ (right). (b) Mott-Schottky plots of CuAlO₂ and Au/CuAlO₂ in aqueous KOH solution purged with N₂ (1 M).





Scheme 1 Schematic band diagrams of CuAlO_2 deposited on (a) FTO and (b) FTO/Au substrates. An energy level arrow (left) shows the electrochemical potentials (*versus* the reversible hydrogen electrode, RHE) for the hydrogen evolution reaction (HER) and oxygen evolution reaction (OER), the conduction band and valence band (CB and VB, respectively) levels, and the work function (W_f) of Au. The W_f values (5.31–5.47 eV) were converted to the electrochemical potential.

a relatively small photocurrent density of $\sim 0.1 \text{ mA cm}^{-2}$ at 0.3 V in the absence of a hole scavenger (Fig. S5†). The addition of the hole scavenger enhanced the photocurrent density to $\sim 0.6 \text{ mA cm}^{-2}$ and the faradaic efficiency to $\sim 100\%$ (Fig. 3c), indicating that the hole transfer was limited. The hole transfer limit was straightforwardly examined by comparing the LSVs of the CuAlO_2 irradiated through the FTO substrate and electrolyte (Fig. S7†). Compared to the substrate-side irradiation, the electrolyte-side irradiation led to significantly reduced photocurrents, even though the light intensity arriving at CuAlO_2 in the substrate side-irradiation was $\sim 80\%$ of the reference light (AM 1.5G; 100 mW cm^{-2}) owing to the semi-transparent FTO (Fig. S8†).³³ Assuming the light penetration depth is the same between the two irradiation directions, the photogenerated holes and electrons under the electrolyte and substrate-side irradiations, respectively, must travel further than their counter charge carriers. Therefore, the reduced photocurrent in the electrolyte-side irradiation reveals that the hole transfer is limited compared to the electron transfer.

3.3. Facilitating hole transfer

To facilitate the hole transfer in water without hole scavengers, a 150 nm-thick Au film was overlaid onto FTO substrates *via* an electron-beam process, onto which CuAlO_2 was electrodeposited. The work function (W_f) of Au is 5.31–5.47 eV,⁴⁴ depending on the surface orientation, which can be estimated to be $\sim 0.3 \text{ V}$ more negative than the CuAlO_2 VB level (Scheme 1b). Accordingly, the Fermi level (E_F) equilibration between the W_f of Au and the E_F of CuAlO_2 causes an enhanced upward band-bending, leading to efficient hole transfer while inhibiting the electron–hole charge recombination. A comparison between the LSVs of the CuAlO_2 samples deposited on bare FTO and FTO/Au (denoted Au/ CuAlO_2) showed that the E_{on} of the latter was $\sim 0.1 \text{ V}$ more negative than that of the former (Fig. 1) because of the upward shift in the E_F of the latter (Scheme 1b). In addition, the presence of the Au underlayer significantly inhibited the dark currents to $E \sim 0.4 \text{ V}$ (Fig. 1), while enhancing the photocurrents (Fig. S9†). The latter was further confirmed by the IPCE profile of Au/ CuAlO_2 , particularly in the range of $\lambda > \sim 450 \text{ nm}$ (Fig. 4a). In contrast to the pristine sample, Au/ CuAlO_2 exhibited an IPCE value of $\sim 10\%$

at $\lambda = 500 \text{ nm}$ and IPCE onset at $\lambda = \sim 800 \text{ nm}$. These enhanced PEC properties could be attributed to the altered energetics produced by the Au underlayer. The Mott–Schottky plot of Au/ CuAlO_2 showed an E_{fb} of $\sim 1.1 \text{ V}$, which was approximately 0.15 V more negative than the E_{fb} of CuAlO_2 (Fig. 4b). Although slightly smaller than the estimated value of $\sim 0.3 \text{ V}$, this shift qualitatively explains the enhanced upward band-bending.

Fig. 5a shows the PEC H_2 production values using Au/ CuAlO_2 films at 0.3 and 0.55 V in an aqueous KOH solution (1 M) without the sulfide/sulfite hole scavengers. The H_2 production rate at 0.3 V was $\sim 2.5 \mu\text{mol h}^{-1}$, three-fold higher than the case of CuAlO_2 (Fig. 3b). The similar amounts of H_2 on the pristine CuAlO_2 at 0.3 V and Au/ CuAlO_2 at 0.55 V (Fig. 3b vs. 5a) indicate that the deposition of the Au underlayer can save 0.25 V. Furthermore, the Au layer enhanced the photocurrent (Fig. S9†), while the faradaic efficiencies were similar ($\sim 100\%$) in these cases ($\text{CuAlO}_2@0.3 \text{ V}$ vs. Au/ $\text{CuAlO}_2@0.55 \text{ V}$) (Fig. 5b).

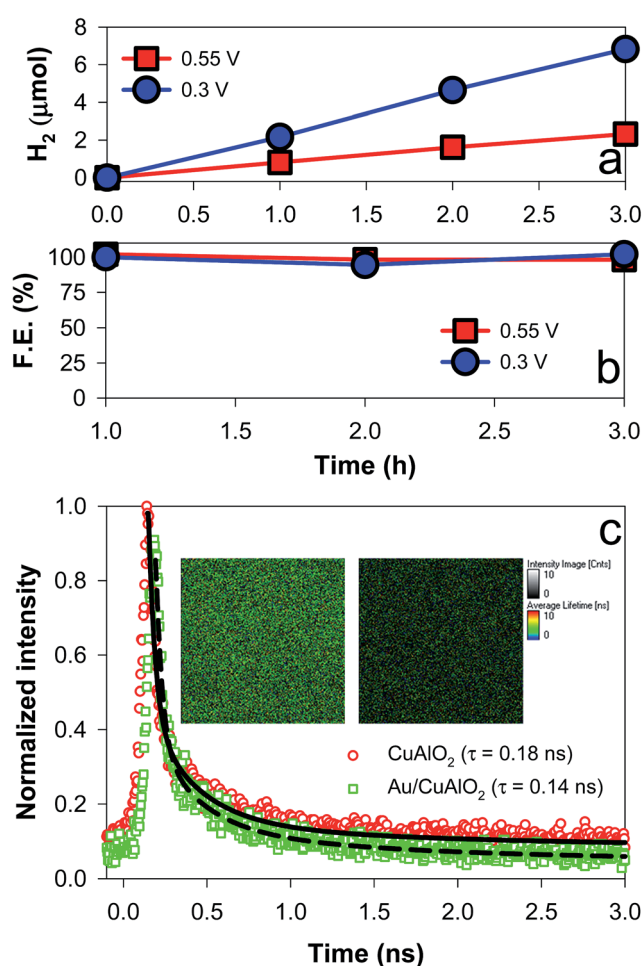


Fig. 5 (a) PEC H_2 production and (b) faradaic efficiencies using Au/ CuAlO_2 electrodes at $+0.3 V_{\text{RHE}}$ and $+0.55 V_{\text{RHE}}$ in aqueous KOH solutions (1 M) purged with N_2 . See Fig. S9† for the time-profiled changes in the photocurrents. (c) Time-resolved photoluminescence emission (500–700 nm) decay spectra of CuAlO_2 and Au/ CuAlO_2 . The average lifetime (τ) is also shown. The inset shows the 2D luminescence intensity and lifetime images of the samples. See Fig. S10–S12† for more information on the emission spectrum.



Accordingly, it is obvious that the Au layer insignificantly influenced the electron injection at the CuAlO₂/water interface, while substantially enhancing the charge separation and transfer.

To examine the charge transfer kinetics and pathways, the time-resolved photoluminescence (TRPL) emission decay spectra of CuAlO₂ and Au/CuAlO₂ samples were compared (Fig. 5c). Prior to the TRPL analysis, the PL emissions of CuAlO₂ and Au/CuAlO₂ were examined in the range of $\lambda > \sim 370$ nm (Fig. S10†). There were no specific emission bands, except for a band at ~ 470 nm. This band is usually found in other oxides and metals, and it could be attributed to the substrate and/or impurities. Accordingly, the samples were excited at $\lambda = 379$ nm, and the long wavelength emission (green emission of 500–700 nm) spectra were primarily compared (see Fig. S11† for the blue emission of 400–500 nm). Upon excitation, the emission intensities of both samples decayed exponentially on a nanosecond time scale, and the average decay time (τ) was estimated by fitting with exponential components (Fig. S11†). As a result, the τ of CuAlO₂ was found to be ~ 0.18 ns, which decreased to ~ 0.14 ns with the Au underlayer (Fig. 5c). When the instrument response was subtracted from the decay profiles, the τ values of CuAlO₂ and Au/CuAlO₂ were estimated to be 1.706 and 1.513 ns, respectively (Fig. S12†). This decrease in τ should have resulted from the charge transfer facilitated by the Au layer, leading to a reduction in the charge recombination. The emission intensity images in the inset of Fig. 5c further confirm the reduced charge recombination on the Au/CuAlO₂ film.

4. Conclusions

We demonstrated that a CuAlO₂ electrode could be readily synthesized *via* an electrodeposition process, and further attempted to enhance the PEC performance of the as-synthesized materials for H₂ production. Whereas CuAlO₂ displayed a similar morphology irrespective of the synthetic conditions (solvent and annealing atmosphere), the electroplating solvent significantly affected the surface properties, crystalline structure, and PEC performance of CuAlO₂. In an alkaline solution, the optimized CuAlO₂ samples showed an E_{on} value of ~ 0.9 V and H₂ production with a faradaic efficiency of $\sim 70\%$ at 0.3 V. The addition of hole-scavengers (sulfide and sulfite) to the solution significantly improved the PEC H₂ production by a factor of 8, and led to a faradaic efficiency of $\sim 100\%$. This strongly suggested that the hole transfer limits the overall PEC performance, which was confirmed by a comparison of the irradiation directions. To facilitate the hole transfer, CuAlO₂ was synthesized on an FTO substrate with a thin Au layer. In the absence of the hole scavengers, the H₂ production with Au/CuAlO₂ was three-fold that with CuAlO₂, while the faradaic efficiencies at 0.3 and 0.55 V were $\sim 100\%$. The TRPL emission decay spectra of CuAlO₂ and Au/CuAlO₂ samples confirmed the facilitated charge transfer in the latter.

Acknowledgements

This research was supported by the Global Research Network Program (2014S1A2A2027802) and the Basic Science Research

Program (2016R1A2B4007366), Korea. In addition, we are grateful to the Korea CCS R&D Center (KCRC) (No. 2014M1A8A1049354) for financial support. This publication was made possible by a grant from the Qatar National Research Fund under its National Priorities Research Program (NPRP 9-052-2-020).

References

- 1 H.-J. Lewerenz and L. Peter, *Photoelectrochemical Water Splitting: Materials, Processes and Architectures*, The Royal Society of Chemistry, Cambridge, 2013.
- 2 K. Maeda and K. Domen, *J. Phys. Chem. Lett.*, 2010, **1**, 2655–2661.
- 3 F. E. Osterloh, *Chem. Soc. Rev.*, 2013, **42**, 2294–2320.
- 4 H. Park, H.-i. Kim, G.-h. Moon and W. Choi, *Energy Environ. Sci.*, 2016, **9**, 411–433.
- 5 J. K. Kim, G. Shin, S. M. Cho, T.-W. Lee and J. H. Park, *Energy Environ. Sci.*, 2011, **4**, 1465–1470.
- 6 S. K. Choi, S. Kim, S. K. Lim and H. Park, *J. Phys. Chem. A*, 2010, **114**, 16475–16480.
- 7 S. K. Choi, W. Choi and H. Park, *Phys. Chem. Chem. Phys.*, 2013, **15**, 6499–6507.
- 8 H. W. Jeong, S. Y. Choi, S. H. Hong, S. K. Lim, D. S. Han, A. Abdel-Wahab and H. Park, *J. Phys. Chem. C*, 2014, **118**, 21331–21338.
- 9 H. W. Jeong, W.-S. Chae, B. Song, C.-H. Cho, S.-H. Baek, Y. Park and H. Park, *Energy Environ. Sci.*, 2016, **9**, 3143–3150.
- 10 Y. K. Kim and H. Park, *Energy Environ. Sci.*, 2011, **4**, 685–694.
- 11 H. Park, Y. K. Kim and W. Choi, *J. Phys. Chem. C*, 2011, **115**, 6141–6148.
- 12 Y. K. Kim and H. Park, *Appl. Catal., B*, 2012, **125**, 530–537.
- 13 H. Park, H. H. Ou, A. J. Colussi and M. R. Hoffmann, *J. Phys. Chem. A*, 2015, **119**, 4658–4666.
- 14 S. K. Choi, U. Kang, S. Lee, D. J. Ham, S. M. Ji and H. Park, *Adv. Energy Mater.*, 2014, **4**, 1301614.
- 15 S. K. Choi, W.-S. Chae, B. Song, C.-H. Choi, J. Choi, D. S. Han, W. Choi and H. Park, *J. Mater. Chem. A*, 2016, **4**, 14008–14016.
- 16 K. Sun, X. Pang, S. Shen, X. Qian, J. S. Cheung and D. Wang, *Nano Lett.*, 2013, **13**, 2064–2072.
- 17 O. Khaselev and J. A. Turner, *Science*, 1999, **280**, 425–427.
- 18 J. Gu, A. Wutting, J. W. Krizan, Y. Hu, Z. M. Detweiler, R. J. Cava and A. B. Bocarsly, *J. Phys. Chem. C*, 2013, **117**, 12415–12422.
- 19 Y. J. Jang, Y. B. Park, H. E. Kim, Y. H. Choi, S. H. Choi and J. S. Lee, *Chem. Mater.*, 2016, **28**, 6054–6061.
- 20 M. S. Prévot, N. Guijarro and K. Sivula, *ChemSusChem*, 2015, **8**, 1359–1367.
- 21 O. Yehezkeli, N. M. Bedford, E. Park, K. Ma and J. N. Cha, *ChemSusChem*, 2016, **9**, 1–9.
- 22 J. Gu, Y. Yan, J. W. Krizan, Q. D. Gibson, Z. M. Detweiler, R. J. Cava and A. B. Bocarsly, *J. Am. Chem. Soc.*, 2014, **136**, 830–833.
- 23 N. Koriche, A. Bouguelia, A. Aider and M. Trari, *Int. J. Hydrogen Energy*, 2005, **30**, 693–699.
- 24 M. S. Prévot, Y. Li, N. Guijarro and K. Sivula, *J. Mater. Chem. A*, 2016, **4**, 3018–3026.



- 25 K. Gurunathan, J.-O. Baeg, S. M. Lee, E. Subramanian, S.-J. Moon and K.-J. Kong, *Catal. Commun.*, 2008, **9**, 395–402.
- 26 A. P. Amrute, Z. Lodziana, C. Mondelli, F. Krumeich and J. Perez-Ramirez, *Chem. Mater.*, 2013, **25**, 4423–4435.
- 27 I. Sullivan, B. Zoellner and P. A. Maggard, *Chem. Mater.*, 2016, **28**, 5999–6016.
- 28 C. G. Read, Y. Park and K.-S. Choi, *J. Phys. Chem. Lett.*, 2012, **3**, 1872–1876.
- 29 U. Kang, S. K. Choi, D. J. Ham, S. M. Ji, W. Choi, D. S. Han, A. Abdel-Wahabe and H. Park, *Energy Environ. Sci.*, 2015, **8**, 2638–2643.
- 30 S. Lee, U. Kang, G. Piao, S. Kim, D. S. Han and H. Park, *Appl. Catal., B*, 2017, **207**, 35–41.
- 31 U. Kang and H. Park, *J. Mater. Chem. A*, 2017, **5**, 2123–2131.
- 32 H. J. Kim, Y.-S. Sohn, C.-d. Kim and D.-h. Jang, *J. Korean Phys. Soc.*, 2016, **69**, 793–797.
- 33 N. C. Deb Nath, S. Y. Choi, H. W. Jeong, J.-J. Lee and H. Park, *Nano Energy*, 2016, **25**, 51–59.
- 34 H. Park, H.-H. Ou, U. Kang, J. Choi and M. R. Hoffmann, *Catal. Today*, 2016, **266**, 153–159.
- 35 S.-H. Hwang, Y. K. Kim, S. H. Yoon, S. K. Lim and H. Park, *RSC Adv.*, 2016, **8**, 85521–85528.
- 36 P. Wang, Y. H. Ng and R. Amal, *Nanoscale*, 2013, **5**, 2952–2958.
- 37 Y. Yang, D. Xu, Q. Wu and P. Diao, *Sci. Rep.*, 2016, **6**, 35158.
- 38 N. de Nevers, *Air Pollution Control Engineering*, McGraw-Hill, New York, 1995.
- 39 H. Park, W. Choi and M. R. Hoffmann, *J. Mater. Chem.*, 2008, **18**, 2379–2385.
- 40 R. Brahim, M. Trari, A. Bouguelia and Y. Bessekhoud, *J. Solid State Electrochem.*, 2010, **14**, 1333–1338.
- 41 N. Benreguia, S. Omeiri, B. Bellal and M. Trari, *J. Hazard. Mater.*, 2011, **192**, 1395–1400.
- 42 T. H. Jeon, A. D. Bokare, D. S. Han, A. Abdel-Wahab, H. Park and W. Choi, *Appl. Catal., B*, 2017, **201**, 591–599.
- 43 S. R. Morrison, *Electrochemistry at Semiconductor and Oxidized Metal Electrodes*, Springer, New York, 1980.
- 44 D. R. Lide, *CRC Handbook of Chemistry and Physics*, CRC Press, New York, 90 edn, 2009.

